Supplementary Information for

Tailoring topological Hall effect in $SrRuO_3/SrTiO_3$ superlattices

Seong Won Cho[a,b,1], Seung Gyo Jeong[c,1], Hee Young Kwon[d], Sehwan Song[e], Seungwu Han[b], Jung Hoon Han[c], Sungkyun Park[e], Woo Seok Choi[c,*], Suyoun Lee[a,f,*], Jun Woo Choi[d,*]

[a] Center for Neuromorphic Engineering, Korea Institute of Science and Technology, Seoul 02792, Korea

[b] Department of Materials Science and Engineering, Seoul National University, Seoul 08826, Korea

[c] Department of Physics, Sungkyunkwan University, Suwon 16419, Korea

[d] Center for Spintronics, Korea Institute of Science and Technology, Seoul 02792, Korea

[e] Department of Physics, Pusan National University, Busan 46241, Korea

[f] Division of Nano & Information Technology, Korea University of Science and Technology, Daejeon 34316, Korea

[1] These authors contributed equally to this work.

* Corresponding Authors. E-mail: choiws@skku.ac.kr (W. S. C.), slee_eels@kist.re.kr (S.L.), junwoo@kist.re.kr (J. W. C.)

Section S1. Thickness characterization of SRO/STO SL

Section S2. Magnetic property of SRO/STO SL

Section S3. ρ_{xy} (H) of SRO/STO SLs with different SRO layer thicknesses

Section S4. Raw data of ρ_{xy} (H) of $[3|8]_z$ SLs at various temperatures

Section S5. Reproducibility of ρ_{xy} (H) data of $[3|8]_z$ SLs

Section S6. Evidence of THE in SRO/STO SL

Section S7. Extraction of THE contribution from ρ_{xy} (H) curves

Section S8. Simulation of the domain evolution with varying DMI and DDI

Section S1. Thickness characterization of SRO/STO SL

Table S1. Supercell structures of $[3|8]_z$ SLs with different z. The thickness of supercell structure is characterized by XRD measurements. The results show a small thickness deviation below 1 unit cell thickness.

*Target-thickness of a supercell is 4.303 nm.

Sample	The measured thickness of supercell (nm)	Deviation (nm)
$[3\|8]_{50}$	4.526	+0.223
$[3\|8]_{20}$	4.147	–0.156
$[3\|8]_{10}$	4.231	–0.072
$[3\|8]_{5}$	4.206	–0.097

Section S2. Magnetic property of SRO/STO SL

The M (T) of the $[3|8]_{10}$ SL along the out-of-plane direction (Fig. S1) shows a typical ferromagnetic (FM) behavior with the transition temperature (T_c) of ~130 K. The M (H) show square-like loops (Fig. S2) supporting mostly homogeneous FM ordering. We note that small anomalies in the M (T) and M (H) curves might be possibly due to a small amount of magnetic inhomogeneity.

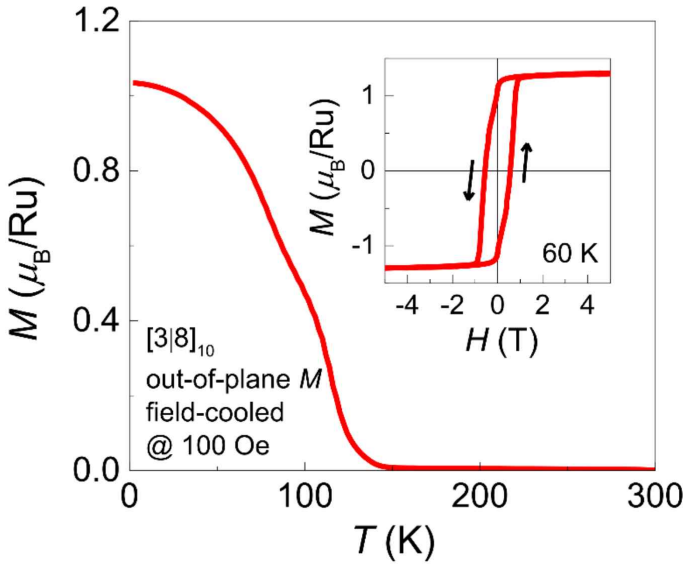

Fig. S1. Ferromagnetic spin ordering of $[3|8]_{10}$ SL. Temperature-dependent field-cooled magnetization (M (T)) of $[3|8]_{10}$ SL along the out-of-plane direction is characterized under a 100 Oe magnetic field. Inset shows magnetic field dependent-magnetization (M (H)) at 60 K, in which the arrows indicate the direction of the magnetic field change.

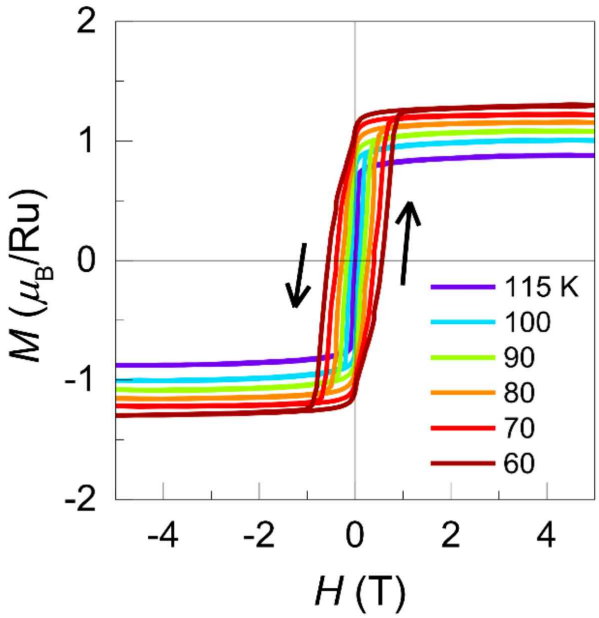

Fig. S2. Out-of-plane M (H) curves of the $[3|8]_{10}$ SL at various temperatures. The arrows indicate the direction of the H-field.

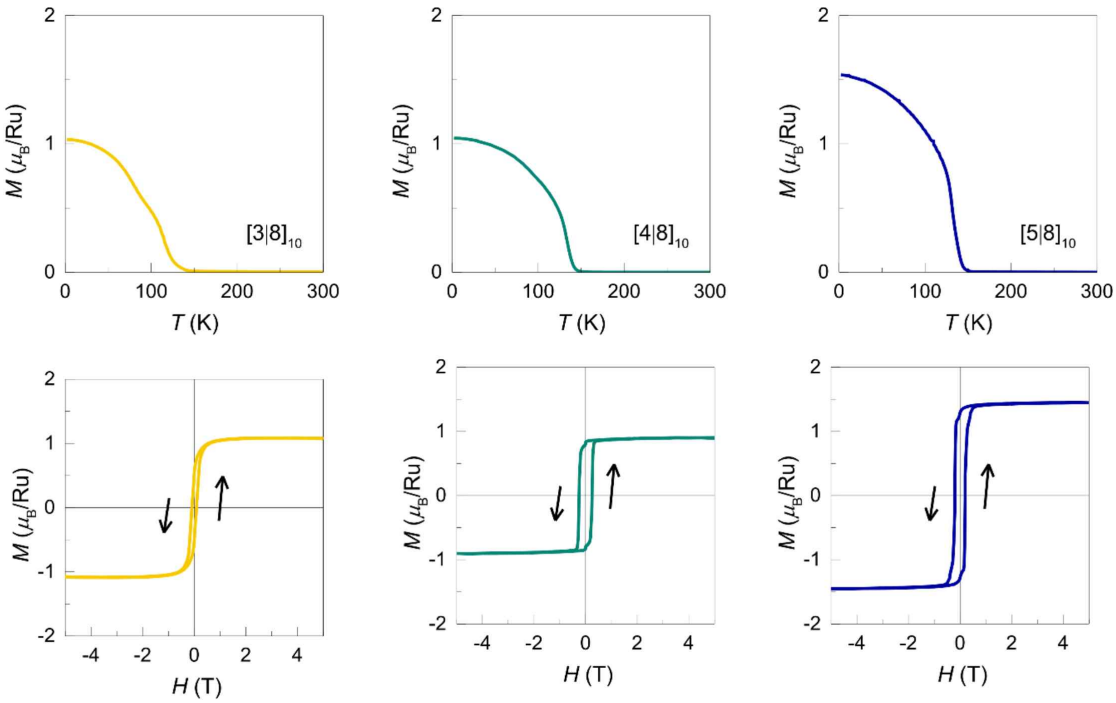

Fig. S3. M (T) and M (H) curves of the $[x|8]_{10}$ SLs. The M (T) curves were measured with 100 Oe of out-of-plane H-fields. The M (H) curves were recorded at 85 K. The arrows indicate the direction of the H-field.

Section S3. ρ_{xy} (H) of SRO/STO SLs with different SRO layer thicknesses

We systematically control the SRO thickness in the $[x|8]_{10}$ SLs (x = 3, 4, and 5) to investigate the x-dependent Hall effect. XRD results of Fig. S4a indicate the atomically well-defined SRO SLs. Figs. S4b-d show the ρ_{xy} (H) curves of the SLs with SRO layers thicker than 3 u.c. ($x \geq 3$). The THE feature is observed only in x = 3 SL, implying the importance of the interface relative to the bulk. In previous reports [1,2], the THE feature was observed in the SRO single layers thicker than 4 u.c. ($x \geq 4$), which is discrepant from our results. This may originate from the fact that the oppositely broken inversion symmetry at the top and bottom interfaces in our SLs suppressed the DMIs, compared with SRO single layers.

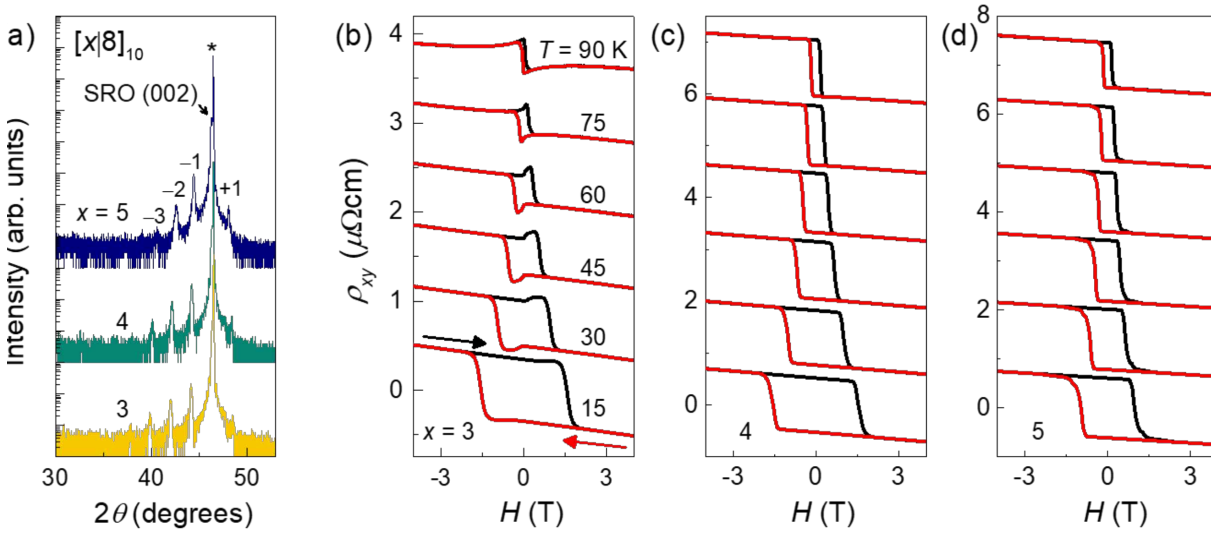

Fig. S4. ρ_{xy} (H) of $[x|8]_{10}$ SLs at various temperatures. (a) XRD θ-2θ scans of $[x|8]_{10}$ SLs show clear SL peaks ($\pm$ n) and their systematic shift in the SLs, indicating atomically well-defined SL periods. (b-d) x-dependent ρ_{xy} (H) curves obtained at various temperatures. Black (red) line indicates the ascending (descending) sweep direction.

Section S4. Raw data of ρ_{xy} (H) of $[3|8]_z$ SLs at various temperatures

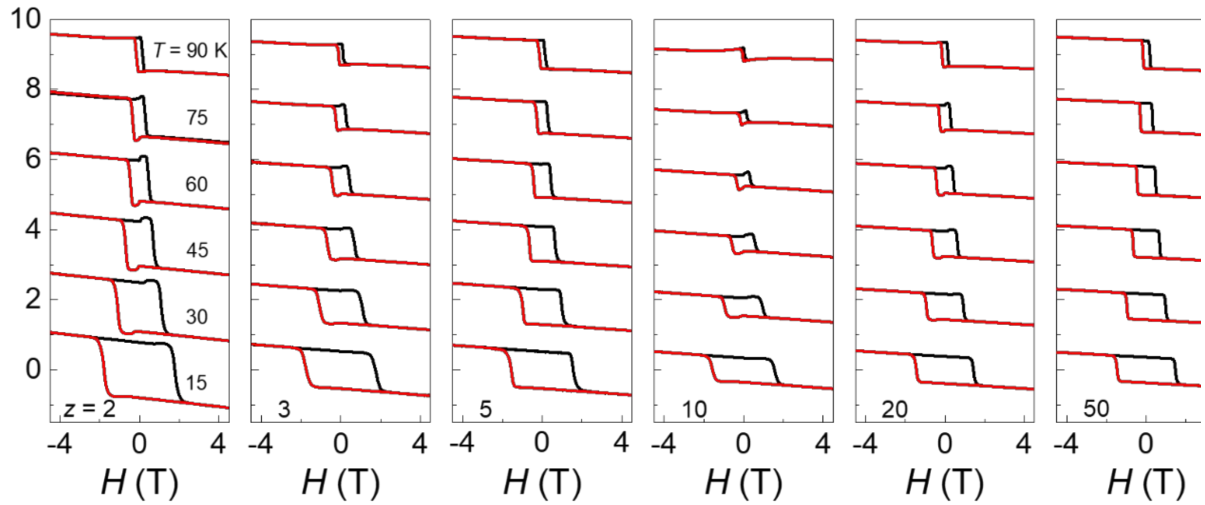

Fig. S5. ρ_{xy} (H) curves of $[3|8]_z$ SLs at various temperatures. Curves are shifted vertically for clarity. Black (red) line indicates the ascending (descending) sweep direction.

Section S5. Reproducibility of ρ_{xy} (H) data of $[3|8]_z$ SLs

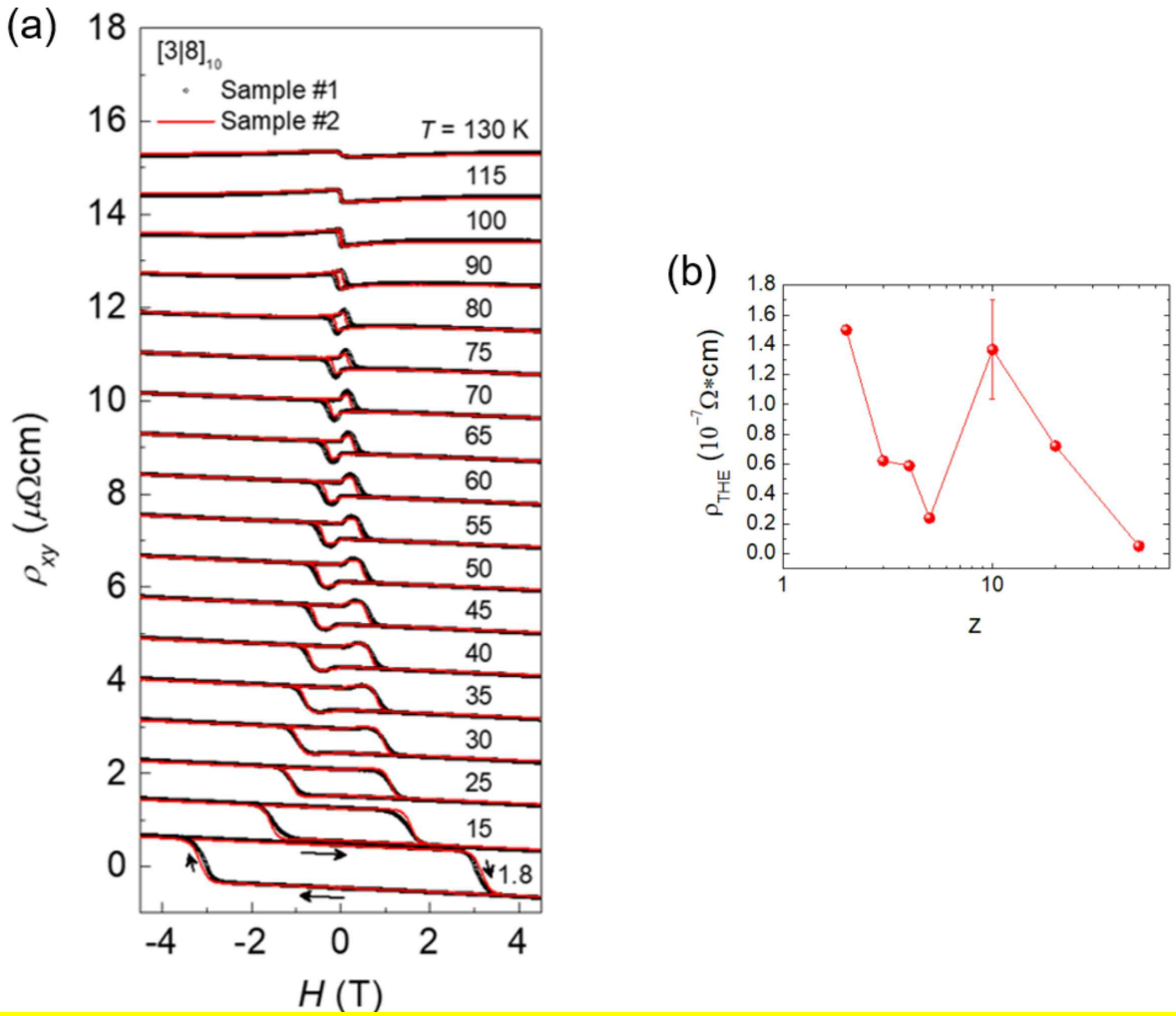

Fig. S6. (a) H-field dependent Hall resistivities (ρ_{xy}) of two different $[3|8]_{10}$ (z = 10) samples. The hollow circle and solid line indicate the ρ_{xy} of two different $[3|8]_{10}$ samples (sample #1 and sample #2). This clearly shows a good reproducibility of our experiments. (b) z-dependence of ρ_{THE} at 60 K with an error-bar for z = 10 samples. The data point and the error-bar represent the average and the max-min values of nominally identical samples, respectively.

Section S6. Evidence of THE in SRO/STO SL

Two distinct models are used to explain the origin of the hump signals: chiral spin textures (THE model) or multiple regions with different coercivities and opposite AHE signs (multi-domain or two-AHE model) [3-6]. Several techniques are used to explicitly distinguish between the two models. In the present study, we can clearly rule out the multi-domain model owing to the points below.

1. The hump-like Hall effect explained by the multi-domain (i.e., two-AHE) model necessarily assumes, and thus always accompanied, a sign change in the AHE for both temperature- and thickness-dependence [3-5]. The sign change in the total AHE around the temperature at which the hump feature is observable is essential in explaining the multi-domain model [7]. In contrast, our SL does not show such temperature-dependent (or in fact, any other parameter dependent) reversal in the sign of AHE, as shown in Figs. S4 and S5.

2. We perform a 'minor-loop' measurement of H-field dependent Hall resistance (R_{xy} (H)), a technique often used to distinguish the two models [3,4,6]. Figs. S7b and S7c schematically represent the distinct H_{min}-dependent minor-loop behavior of our SLs following the THE model and the multi-domain model. The measured data in Fig. S7a, which shows a very narrow hysteresis for small $H_{min,}$ better agrees with the THE model (Fig. S7b). Furthermore, whereas the hump-like Hall resistivity of multi-domain models shows asymmetric behavior depending on the sign of H-field (Fig. S7c) [3], our SLs show a symmetric Hall resistivity behavior as a function of H-field (Fig. S7a). Additionally, the hump-like Hall resistivity values of multi-domain models increase as increasing with H_{min} [3]. In contrast, the inset of Fig. S7a shows identical THE values for our SL regardless of H-field.

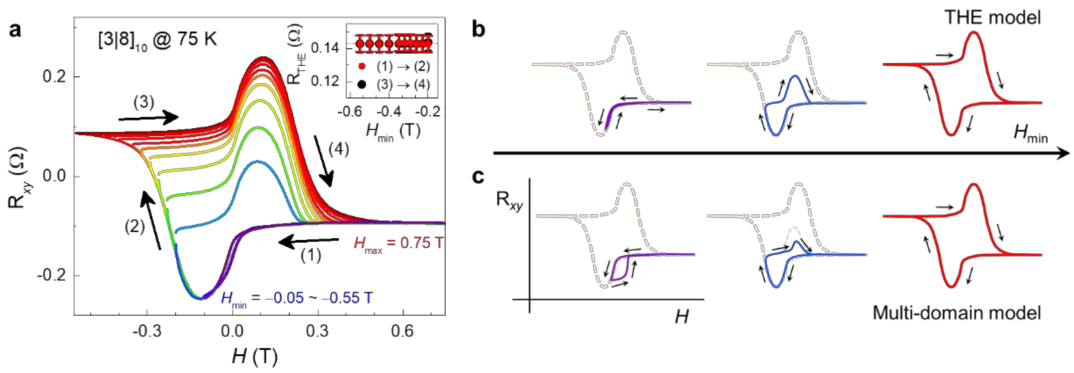

Fig. S7. 'Minor-loop' measurements of $[3|8]_{10}$ SL at 75 K. (a) R_{xy} vs. H curves, which are measured by fixing the maximum positive H-field (H_{max}) at 0.75 T and varying the minimum negative H-field (H_{min}) from –0.05 to –0.55 T. The inset shows the nearly same R_{THE} values regardless of H_{min} and sign of H-field. We extracted R_{THE} for two different sweep direction of H-field. Schematics of H_{min}-dependent minor loops for (b) THE and (c) multi-domain model. The arrows indicate the sweep direction of the H-field.

3. Thickness inhomogeneity of SRO is the origin of the multi-domain model. That is, a superposition of two electrical Hall channels, which have opposite Hall signs and different coercivities, might lead to the hump-like Hall effect. In particular, inhomogeneities between 4 and 5 u.c.-thick SRO single layer or thicker usually showed the hump-like Hall effect originating from the multi-domain model [3,5]. However, the excellent thickness control evidenced by the XRD analyses (Fig. 1c) leads us to believe we have uniform SRO thickness in our SL samples. Furthermore, it is unconceivable that any inhomogeneity would have strong z-dependence, such that magnetic inhomogeneity in itself cannot fully explain the nonmonotonic z-dependence of the THE.

4. Finally, the multi-domain models cannot describe the nonmonotonic z-dependent THE observed in the SLs. The nonmonotonic z-dependence of the THE indicates the presence of two competing terms that scale differently with z, ruling out the two-AHE model as the origin. In particular, when z = 50, negligibly small THE and clear hysteresis in the AHE

was observed; according to the two-AHE model, the hump signal should exist independent of z.

Section S7. Extraction of THE contribution from ρ_{xy} (H) curves

In Fig. S8a, the raw ρ_{xy} of $[3|8]_4$ SL is plotted as a function of H-field at 80 K, clearly showing a nonlinear dependence of the ordinary Hall effect (OHE) on the H-field. To estimate the THE contribution more accurately, separating the nonlinear ρ_{OHE} from the raw ρ_{xy} is important. As such a nonlinear ρ_{OHE} is believed to originate from the coexistence of electrons and holes in our SL samples [8], ρ_{OHE} is separated using the following two-step process: (1) removal of the anomalous Hall effect (AHE) contributions and (2) fitting by the two-band model [9]. The AHE signal, which is proportional to the magnetization M, is assumed to be a square-like hysteresis loop with a well-defined coercive field (H_{c}) based on the M (H) measurements (Fig. S2). Hence, the AHE contribution is removed by adding an offset (step function) to the raw ρ_{xy} outside H_{c} such that the shifted ρ_{xy} vs. H curve crosses the origin, as shown in Figure S8a. The resulting ρ_{xy} (H) curve outside H_{c} is fitted using the two-band model, resulting in the contribution from the nonlinear ρ_{OHE} inside H_{c}. Fig. S8b shows a comparison between two ($\rho_{xy} - \rho_{\mathrm{OHE}}$) vs. H curves, where each curve is obtained with and without considering the nonlinear ρ_{OHE}, separately. The hump for the curve assuming a nonlinear ρ_{OHE} is localized near H_{c}, whereas it extends far beyond H_c for the curve assuming a linear ρ_{OHE}, resulting in an incorrect estimation of the THE.

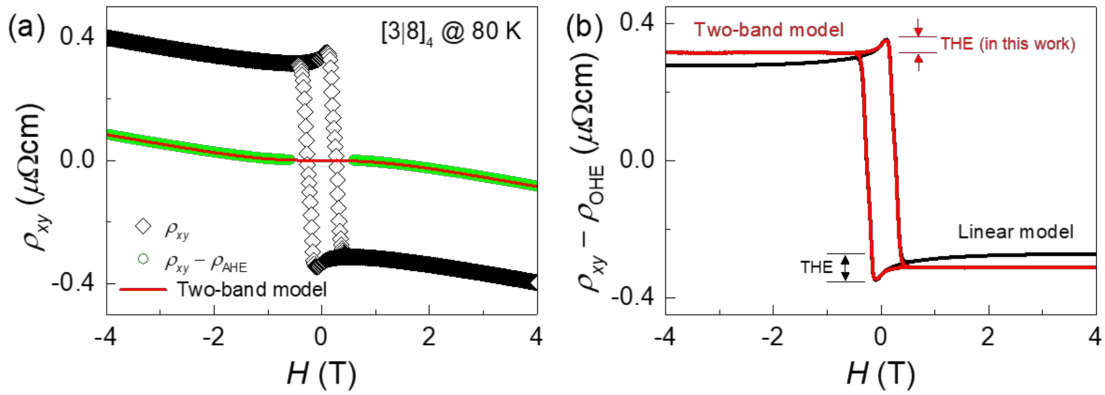

Fig. S8. Extraction of THE contribution from ρ_{xy} (H) curves. (a) Raw ρ_{xy} vs. H curve of $[3|8]_4$ SL at 80 K (black open diamond), ($\rho_{xy} - \rho_{\mathrm{AHE}}$) vs. H curve outside the coercive field, obtained by removing an offset to cross the origin (green circle), and two-band model fitting to ($\rho_{xy} - \rho_{\mathrm{AHE}}$) vs. H curve (solid red line). (b) Comparison of the two models to determine the THE contributions: linear OHE model (black) and nonlinear OHE using a two-band model (red).

Section S8. Simulation of the domain evolution with varying DMI and DDI

We consider an SL system where the DMI and long-range DDI scale with $1/z$ and z, respectively. The latter is a natural assumption for thin films in general [10,11], as the DDI *energy per area* is proportional to M^2 (M: magnetization) and in turn to z^2, and, therefore, the DDI *energy per volume* is proportional to z. In addition, in our symmetric SL system, the DMI originates from only the very bottom SRO/STO interface (see discussion below), such that the interfacial DMI remains constant regardless of z. Nevertheless, the DMI energy would affect the whole SL system owing to the bottom-most SRO being strongly ferromagnetic coupled to the other SRO layers. Thus, the effective DMI energy acting on the SL system is obtained by dividing the z-independent DMI by the volume of the SL ($\sim z$), such that the DMI *energy per volume* $\sim 1/z$.

In designing the above model, we make two assumptions: (i) a ferromagnetic interlayer coupling between the perpendicular magnetizations of the different SRO layers, and (ii) the presence of interfacial DMI. We justify the two assumptions below.

First, we consider the out-of-plane interlayer interaction between the different SRO layers in our SL system. In numerous earlier experimental studies on magnetic multilayer systems, it was shown that the ferromagnetic layers were strongly dipolar coupled across thick (2-7 nm) non-magnetic layers. This resulted in the formation of perpendicular 2D spin textures such as skyrmions [12-16]. Particularly in Ref. 14, it was explicitly shown that all the CoFeB layers in a Pt/CoFeB/MgO multilayer system have identical spin textures. Therefore, it is reasonable to believe that there would be an out-of-plane ferromagnetic interlayer coupling.

The next open question is the origin of the DMI in our SL system. First, note that DMI naturally appears for systems with broken inversion symmetry and strong spin-orbit coupling. The latter is already well established in previous references. For example, the existence of

large spin-orbit coupling has been reported in STO-related systems [17-19]. Moreover, the role of spin-orbit coupling of the Ru ions has been the essence of most SRO related studies for decades. In particular, some studies explicitly show interfacial DMI originating solely from the SRO/STO interface [1,20]. We also argue that inversion symmetry breaking necessary for the DMI, can exist even in our ideally symmetric SRO/STO SL system. Our SL system has a coherent structure for all z values (see Figs. 1b-d in main text), which would ideally maintain the inversion symmetry. Therefore, the DMI at the two repeated interfaces, i.e. SRO/STO and STO/SRO, would cancel out each other. However, it is conceivable that the DMI at the bottom-most interface, i.e. SRO//STO (substrate), may have a magnitude that differs from those of the SRO/STO(film) interfaces as the inversion symmetry breaking would be the most severe in the bottom-most SRO layer adjacent to the STO substrate (see schematics in main text Figure 1a). In fact, a previous study regarding spin chirality in epitaxially grown symmetric SL systems not only revealed a sizeable DMI, but also the sign and size of the DMI could be altered by slightly modifying the bottom-most layer thickness [21]. This directly supports our argument that the SRO//STO(substrate) and SRO/STO(film) interface might have different DMIs. In this scenario, only the DMI at the SRO//STO(substrate) interface would be non-cancelling such that the DMI would scale with $1/z$, as previously postulated. Meanwhile, the DDI would still scale with z, as described earlier.

Micromagnetic simulations are performed using the Monte-Carlo method with a 2D square grid system and Heisenberg model, which has been used in many studies to investigate 2D magnetic domains [11,22]. As mentioned in the beginning of this section, the long-range DDI *energy per volume* scales with z. Meanwhile, the demagnetization energy induced by the dipolar interaction is proportional to the volume of the system. Hence, the demagnetization *energy per volume* is z invariant. For the accurate matching of our

simulation model to the experimental system, we separated the demagnetization energy from the long-range DDI and included it into the effective perpendicular magnetic anisotropy (PMA) in the form of a shape anisotropy, as expressed as follows:

$$\begin{aligned} & J\sum_{<ij>}\vec{S}_i\cdot\vec{S}_j - K_z\sum_i S_{i,z}{}^2 - \sum_{<ij>}\vec{\beta}_{ij}\cdot\vec{S}_i\times\vec{S}_j - D\sum_{ij}\frac{3(\vec{S}_i\cdot\vec{r}_{ij})(\vec{S}_j\cdot\vec{r}_{ij}) - \vec{S}_i\cdot\vec{S}_j|\vec{r}_{ij}|^2}{|\vec{r}_{ij}|^5} - h_z \\ & j - K_{eff,z}\sum_i S_{i,z}{}^2 - \sum_{<ij>}\vec{\beta}_{ij}\cdot\vec{S}_i\times\vec{S}_j - D\sum_{ij}\frac{3(\vec{S}_i\cdot\vec{r}_{ij})((\vec{S}_j-\vec{S}_i)\cdot\vec{r}_{ij}) - \vec{S}_i\cdot(\vec{S}_j-\vec{S}_i)|\vec{r}_{ij}|^2}{|\vec{r}_{ij}|^5} \end{aligned} \quad \text{(S1)}$$

Here J, β $(=|\vec{\beta}_{ij}|)$, K_z, $K_{eff,z}$, D, and h_z are the scaled parameters for the exchange interaction, DM interaction, PMA, effective PMA $(= K_z - K_{shape})$, magnetic dipole interaction, and external out-of-plane magnetic field, respectively. Note that in the second expression of Eq. (S1), the demagnetization energy of a 2D ferromagnetic film system with a uniform magnetic domain, $D\sum_{ij}\frac{3(\vec{S}_i\cdot\vec{r}_{ij})^2 - |\vec{S}_i|^2|\vec{r}_{ij}|^2}{|\vec{r}_{ij}|^5}$, is included in the effective PMA ($K_{eff,z}$), since the term can be considered as a form of shape anisotropy, K_{shape} $(= 2\pi D)$ [10]. To simplify the calculations, in our model, the spin on a grid site $\vec{S}$ is set as a unit vector, and the $\vec{r}_{ij}$ in the dipole interaction is set as a dimensionless displacement vector.

The relations used to obtain the spin configurations are expressed as follows:

$$\begin{aligned} |\vec{S}_{//\vec{h}_{eff}}| &= \frac{T\log\left[\exp\left(-\frac{|\vec{h}_{eff}|}{T}\right) + 2R\times\sinh\left(\frac{|\vec{h}_{eff}|}{T}\right)\right]}{|\vec{h}_{eff}|} \\ |\vec{S}_{\perp\vec{h}_{eff}}| &= \sqrt{1 - |\vec{S}_{//\vec{h}_{eff}}|^2} \end{aligned} \quad \text{(S2)}$$

Here R is a random number, T is the temperature parameter, and $\vec{h}_{eff}$ is the effective magnetic field $\left(=\frac{\partial \mathcal{H}}{\partial \vec{S}_i}\right)$. Moreover, $\vec{S}_{//\vec{h}_{eff}}$ and $\vec{S}_{\perp\vec{h}_{eff}}$ are spin components along and perpendicular to $\vec{h}_{eff}$, respectively.

The z-dependent magnetic domains are shown in Fig. S9, with representative magnetic domain images shown in main text Fig. 3c. The scaled Hamiltonian parameters used to obtain Fig. 3c and Fig. S9 are set to $J = 1$, $K_{eff,z} = 0.04$, and $h_z = 0.007$, whereas β and D changed with z : $\beta = \left|\vec{\beta}_{ij}\right| = \frac{\beta_0}{z} = \frac{0.45}{z}$ and $D = D_0 z = 0.008z$.

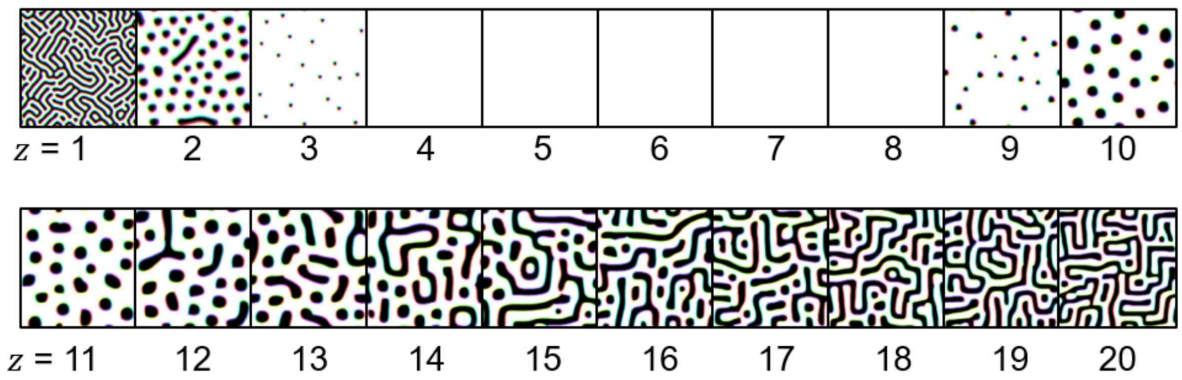

Fig. S9. Repetition number (z)-dependent modulation of the spin texture (z = 1 − 20) obtained using the Monte-Carlo method. A Néel-type skyrmion phase at z = 2 and 3, and a Bloch-type skyrmion phase at z = 9 −12 are observed, with a phase with no domains (uniform magnetization) in between. Worm-shaped and magnetic-stripe domains form with further increase in z.

The choice of $\beta_0 = 0.45$ is based on estimations from experimental values in the literature. In a SRO system, the magnitude of J and K_z are reported to be ~ 20 meV and ~ 0.26 meV, respectively [23,24]. The critical condition determining whether chiral structures

induced by DMI can be stabilized is $\beta \approx \sqrt{JK_z}$. [25,26], which gives $\beta \approx 2.3$ meV in the SRO system. As mentioned in our manuscript, since we speculate that β of our SL system is modulated by the repetition number z ($\beta = \beta_0/z$), β_0 can be estimated if an appropriate number of z is found that satisfies the critical condition mentioned above. In our experimental results, we see that the THE signal is greatly reduced when $z \sim 4$. We speculate that this is caused by the annihilation of magnetic skyrmions formed by DMI, and thus we estimate that $\beta_0 \approx 9.2$ meV ($\beta_0/4 \approx 2.3$ meV), such that $\beta_0/J \approx 9.2 / 20 \approx 0.46$. This justifies the $\beta_0 = 0.45$ used in the simulations (we have set $J = 1$, i.e. all the parameters are normalized to J).

On the other hand, a quantitative comparison between the DDI strengths (D) in experiments and simulations, is non-trivial. For instance, the thickness of STO spacers in the SL can influence the DDI in our simple two-dimensional simulation model, yet it is difficult to quantify its effect by experimental measurements. Alternatively, we perform additional simulations that show the unique phase transition behavior (DMI skyrmion → uniform → DDI skyrmion) appearing in a wide range of D_0 values ($D_0 = 0.006 – 0.010$), which are shown in Fig. S10. This implies that the *z*-dependent modulation of the magnetic skyrmion phase is robust, and consistently appear even when other D_0 values are used for the simulations.

We emphasize that the domain images should only be interpreted qualitatively, since the simulations were done with scaled parameters, not actual parameters derived from experimental measurements. For instance, in order to form DDI stabilized domains in the simulation image (a finite system), the relative strength of the long-range DDI used in the simulations is possibly larger than those in the continuous film (roughly corresponding to an infinite 2D system) used for the experiments. Thus, the simulated DDI skyrmion size might be smaller than its actual size.

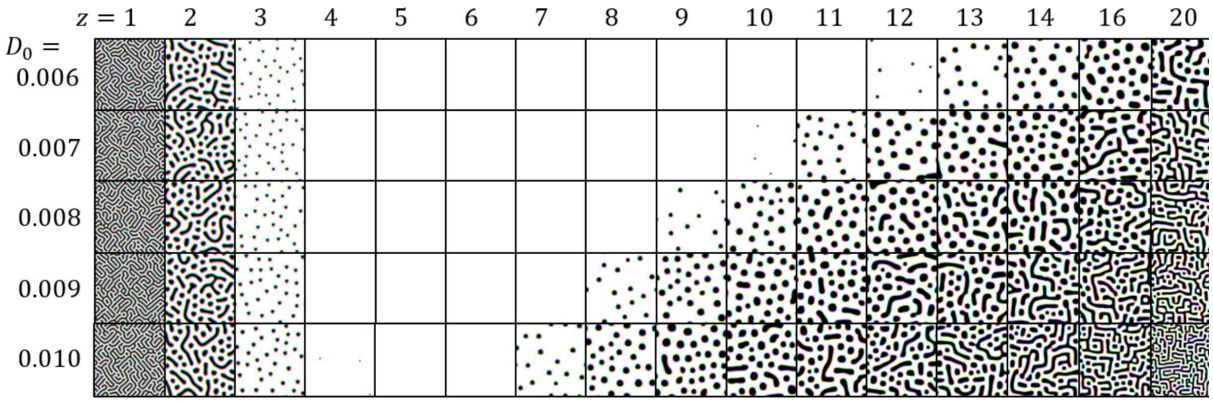

Fig. S10. Repetition number (z)-dependent modulation of the spin texture for D_0 = 0.006 – 0.010. The other simulation parameters are fixed ($K_{eff,z}$= 0.04, β_0= 0.45, h = 0.007).

The DMI skyrmion – uniform – DDI skyrmion phase transition appears for all D_0 values.

References

[1] Q. Qin, L. Liu, W. Lin, X. Shu, Q. Xie, Z. Lim, C. Li, S. He, G.M. Chow, J. Chen, Emergence of Topological Hall Effect in a $SrRuO_3$ Single Layer, Adv. Mater. 31 (2019) 1807008.

[2] L. Wang, Q. Feng, Y. Kim, R. Kim, K.H. Lee, S.D. Pollard, Y.J. Shin, H. Zhou, W. Peng D. Lee, W. Meng, H. Yang, J.H. Han, M. Kim, Q. Lu, T.W. Noh, Ferroelectrically tunable magnetic skyrmions in ultrathin oxide heterostructures, Nat. Mater. 17 (2018) 1087-1094.

[3] D. Kan, T. Moriyama, K. Kobayashi, Y. Shimakawa, Alternative to the topological interpretation of the transverse resistivity anomalies in $SrRuO_3$, Phys. Rev. B 98 (2018) 180408.

[4] P.-C. Wu, H. Song, Y. Yuan, B. Feng, Y. Ikuhara, R. Huang, P. Yu, C.-G. Duan, Y.-H. Chu, Thickness dependence of transport behaviors in $SrRuO_3/SrTiO_3$ superlattices, Phys. Rev. Mater. 4 (2020) 014401.

[5] L. Wang, Q. Feng, H. G. Lee, E. K. Ko, Q. Lu, T. W. Noh, Controllable Thickness Inhomogeneity and Berry Curvature Engineering of Anomalous Hall Effect in $SrRuO_3$ Ultrathin Films, Nano Lett. 20 (2020) 2468-2477.

[6] B. M. Ludbrook, G. Dubuis, A. H. Puichaud, B. J. Ruck, S. Granville, Nucleation and annihilation of skyrmions in Mn_2CoAl observed through the topological Hall effect, Sci. Rep. 7 (2017) 13620.

[7] L. Wu, Y. Zhang, arXiv:1812.09847v6 (2020).

[8] S.G. Jeong, T. Min, S. Woo, J. Kim, Y.-Q. Zhang, S.W. Cho, J. Son, Y.-M. Kim, J.H. Han, S. Park, H.Y. Jeong, H. Ohta, S. Lee, T.W. Noh, J. Lee, W.S. Choi, Phase Instability amid Dimensional Crossover in Artificial Oxide Crystal, Phys. Rev. Lett. 124 (2020) 026401.

[9] N.W. Ashcroft, N.D. Mermin, Solid State Physics, Holt, Rinehart and Winston, New York, 1976.

[10] Y. Yafet, E.M. Gyorgy, Ferromagnetic strip domains in an atomic monolayer, Phys. Rev. B 38 (1988) 9145-9151.

[11] H.Y. Kwon, K.M. Bu, Y.Z. Wu, C. Won, Effect of anisotropy and dipole interaction on long-range order magnetic structures generated by Dzyaloshinskii–Moriya interaction, J. Magn. Magn. Mater. 324 (2012) 2171-2176.

[12] S. Woo, K. Litzius, B. Krüger, M.-Y. Im, L. Caretta, K. Richter, M. Mann, A. Krone, R.M. Reeve, M. Weigand, P. Agrawal, I. Lemesh, M.-A. Mawass, P. Fischer, M. Kläui, G.S.D. Beach, Observation of room-temperature magnetic skyrmions and their current-driven dynamics in ultrathin metallic ferromagnets, Nat. Mater. 15 (2016) 501-506.

[13] C. Moreau-Luchaire, C. Moutafis, N. Reyren, J. Sampaio, C.A.F. Vaz, N. Van Horne, K. Bouzehouane, K. Garcia, C. Deranlot, P. Warnicke, P. Wohlhüter, J.M. George, M. Weigand, J. Raabe, V. Cros, A. Fert, Additive interfacial chiral interaction in multilayers for stabilization of small individual skyrmions at room temperature, Nat. Nanotechnol. 11 (2016) 444-448.

[14] S. Woo, K.M. Song, H.-S. Han, M.-S. Jung, M.-Y. Im, K.-S. Lee, K.S. Song, P. Fischer, J.-I. Hong, J.W. Choi, B.-C. Min, H.C. Koo, J. Chang, Spin-orbit torque-driven skyrmion dynamics revealed by time-resolved X-ray microscopy, Nat. Commun. 8 (2017) 15573.
[15] A. Soumyanarayanan, M. Raju, A. L. Gonzalez Oyarce, A. K. C. Tan, M.-Y. Im, A. P. Petrović, P. Ho, K. H. Khoo, M. Tran, C. K. Gan, F. Ernult, C. Panagopoulos, Tunable room-temperature magnetic skyrmions in Ir/Fe/Co/Pt multilayers, Nat. Mater. 16 (2017) 898-904.
[16] M. Raju, A. Yagil, A. Soumyanarayanan, A.K.C. Tan, A. Almoalem, F. Ma, O.M. Auslaender, C. Panagopoulos, The evolution of skyrmions in Ir/Fe/Co/Pt multilayers and their topological Hall signature, Nat. Commun. 10 (2019) 696.
[17] W. Lin, L. Li, F. Doğan, C. Li, H. Rotella, X. Yu, B. Zhang, Y. Li, W. S. Lew, S. Wang, W. Prellier, S. J. Pennycook, J. Chen, Z. Zhong, A. Manchon, T. Wu, Interface-based tuning of Rashba spin-orbit interaction in asymmetric oxide heterostructures with 3d electrons, Nat. Commun. 10 (2019) 3052.
[18] M. Liu, Y. Hong, H. Xue, J. Meng, W. Jiang, Z. Zhang, J. Ling, R. Dou, C. Xiong, L. He, J. Nie, Enhancement of Rashba spin–orbit coupling by electron confinement at the $LaAlO_3/SrTiO_3$ interface, J. Phys.: Condens. Matter 2020, 32, 235003.
[19] M. Briggeman, J. Li, M. Huang, H. Lee, J.-W. Lee, K. Eom, C.-B. Eom, P. Irvin, J. Levy, Engineered spin-orbit interactions in $LaAlO_3/SrTiO_3$-based 1D serpentine electron waveguides, Sci. Adv. 48 (2020) eaba6337.
[20] H. Huang, B. Kim, B. Shon, C. Kim, C.-C. Kao, J.-S. Lee, Detection of the Chiral Spin Structure in Ferromagnetic $SrRuO_3$ Thin Film. ACS Appl. Mater. Interfaces 33 (2020) 37757-37763.
[21] G. Chen, T. Ma, A. T. N'Diaye, H. Kwon, C. Won, Y. Wu, A. K. Schmid, Tailoring the chirality of magnetic domain walls by interface engineering, Nat. Commun. 4 (2013) 2671.
[22] H. Y. Kwon, S. S. Hong, J. H. Seok, K. M. Bu, Y. Z. Wu, Z, Q. Qiu, C. Won, A study of the stripe domain phase at the spin reorientation transition of two-dimensional magnetic system, J. Magn. Magn. Mater. 322 (2010) 2742-2748.
[23] A. Kanbayasi, Magnetocrystalline Anisotropy of $SrRuO_3$, J. Phys. Soc. Jpn. 41 (1976) 1879-1883.
[24] J. Matsuno, N. Ogawa, K. Yasuda, F. Kagawa, W. Koshibae, N. Nagaosa, Y. Tokura, M. Kawasaki, Interface-driven topological Hall effect in $SrRuO_3$-$SrIrO_3$ bilayer, Science Advances 2 (2016) e1600304.
[25] A. N. Bogdanov, D. A. Yablonskii, Thermodynamically stable "vortices" in magnetically ordered crystals. The mixed state of magnets, Zh. Eksp. Teor. Fiz 95 (1989) 178-182.
[26] A. Bogdanov, A. Hubert, J. Magn. Magn. Mater. 138 (1994) 255-269.